To cite this version :

Michel AULELEY, Hervé MAHE, Olivier THOMAS, Christophe GIRAUD-AUDINE - Tunable electromagnetic resonant shunt using pulse-width modulation - Journal of Sound and Vibration - Vol. 500, p.116018 - 2021

Tunable electromagnetic resonant shunt using pulse-width modulation

Michel AULELEY[♯,♮] **and Christophe GIRAUD-AUDINE**[♭] **and Hervé MAHÉ**[♮] **and Olivier THOMAS**[♯]

[♯]Arts et Metiers Institute of Technology, LISPEN, HESAM Université, F-59000 Lille, France

[♭]Arts et Metiers Institute of Technology, Univ. Lille, Centrale Lille, HEI, HESAM Université, L2EP - Laboratoire d'Électrotechnique et d'Électronique de Puissance, F-59000 Lille, France

[♮]Valeo Transmissions, Centre d'Étude des Produits Nouveaux Espace Industriel Nord, Route de Poulainville, 80009 Amiens Cedex 1, France

E-mail: `olivier.thomas@ensam.eu`

Abstract.

This article proposes a novel mean for tuning the natural frequency of an electromagnetic resonant shunt, using a pulse-width modulation (PWM) circuit. It is used to modulate the value of the capacitance of the shunt, and the electrical frequency is shown to be proportional to the command parameter of the PWM, the duty cycle. An easy and efficient strategy to tune the resonant shunt in real time is then proposed, thus obtaining a low powered and always stable vibration control device. The article proposes the theory of PWM, giving a robust method to predict the dynamics of the system. Then, an accurate multi-mode theoretical model of the tunable resonant shunt coupled to an elastic structure is proposed and experimentally validated on an elastic multi-mode structure, in the case of two different control strategies. The first one is a standard resonant shunt with both the electrical frequency and damping optimized to reduce a given resonance peak. The second one is based on a resonant shunt with the electrical damping as low as possible, which creates an antiresonance and a "notch" type mechanical response at the driving frequency. Both strategies are experimentally validated with real time variation and adaptation of the electrical frequency, obtaining an efficient vibration control device, able to reduce by a factor 40 the vibration level.

1. Introduction

The search for increasing performance, acoustic comfort and fatigue life of mechanical systems and structures often necessitates the design of vibration reduction systems. Apart from including special passive damping materials into the structure, such as viscoelastic polymers or foams [1, 2, 3], the use of mechanical vibration absorbers such as dynamic vibration absorbers (DVAs) or Lanchester dampers [4, 5] is common. Equivalent damping properties can be obtained using electromechanical shunts, in which

a transducer converts the vibratory energy of the host structure into electrical energy in a dedicated electronic circuit, designed to dissipate it and/or to counteract the structure's vibrations. Depending on the physics of the transducer, piezoelectric or electromagnetic shunts have been proposed in the pioneering works [6, 7], and have been addressed in a huge number of contribution since (see [8, 9] and reference therein).

Using a DVA or a resonant shunt (its electromechanical equivalent), two practical issues are often addressed, depending on the type of the excitation signal. (i) If it has a broadband frequency content, one is often interested in attenuating as much as possible one or several resonances of the host structure. Depending on the figure of merit of the absorber (the mass ratio for the DVA; the electromechanical coupling factor for the shunts) and the damping ratio of the considered mechanical mode, substantial vibration reduction can be obtained on a single resonance [5, 9, 10, 11]. Several resonances can also be attenuated with more complex circuits [12]. (i) For a tonal excitation signal, DVAs and resonant shunts, damped as less as possible, can be efficiently used to almost cancel the vibration energy by creating an antiresonance at the absorber natural frequency [9]. In those two cases of broadband or tonal excitation signal, the fine tuning of the absorber natural frequency, either on a particular host structure resonance or on the excitation frequency, is mandatory. This has stimulated the interest in designing adaptive absorbers, which can self-tune by adaptively changing some of their parameters. This article addresses a novel strategy for tuning the natural frequency of an electromagnetic resonant shunt, using an electronic chopper with pulse-width modulation (PWM). This technology is well known and used in power electronics technologies to regulate the power flowing in a circuit, thanks to electronic components switched at a high frequency [13, 14]. In this paper, this principle is adapted to modify the characteristics of a resonant circuit.

In designing an adaptive shunt, one has to deal with two issues. First, one has to provide a technology able to change the shunt natural frequency to a desired value. Next, a suitable shunt tuning control strategy must be formulated. The pioneering works in this field were proposed for piezoelectric transduction in [15, 16]. The former proposed to change the electrical natural frequency using a motorized variable resistor included in the synthetic inductor of the shunt; the control law was based on the minimization of the root mean square (RMS) value of the vibration signal. In the latter, the authors use a simple capacitive shunt constituted of a ladder of discrete capacitor controlled by switches, to adapt the capacitance value and change the equivalent stiffness of a mechanical absorber. An additional step was proposed in [17], with a synthetic impedance based on a real-time digital signal processor (DSP), which can be easily tuned by changing the parameters of the block diagram in the DSP. The control law was based on the RMS value of the vibration signal. An important update was proposed in [18], with an analog tunable inductance including a voltage controlled resistor and a new control law based on the phase of the shunt impedance. This control law was adapted to multi-mode damping in [19], with a DSP-based shunt impedance. Those techniques, all based on piezoelectric transduction, were applied to an electromagnetic shunt for the first time in [20]. Since

then, we can notice three interesting updates with analog electronic circuits, in the case of piezoelectric shunts [21, 22, 23] (with a fully analog circuit including junction gate field-effect transistors in the first, a photoresistive opto-isolator with a phase locked loop processor in the second and a digital potentiometer in the third). The so-called sweeping and switching technique, that uses an adaptive piezoelectric shunt impedance, was also proposed for broadband vibration damping (see [24] and reference therein). Recently, programmable digital shunts have also been proposed [25, 26]. For electromagnetic transduction, some tunable DVAs, with a variable capacitance to change their apparent stiffness, where proposed in [27, 28]. However, it seems that no contribution on adaptive resonant electromagnetic shunts has been proposed since the pioneering work [20].

It is worth to notice the so-called synchronized switch damping (SSD) techniques which are also intrinsically adaptive. They consist in switching the electromechanical transducer on two distinct shunt impedances, synchronously with the oscillations of the host structure. This idea was initially proposed in [29, 30] for piezoelectric transduction and developed in numerous contributions since then (see [31] for a recent review). SSD techniques in the case of electromagnetic transduction were first proposed in [32]. Those SSD techniques are very interesting since they appear adaptive, efficient, intrinsically stable and require low power. Their effect can be viewed as a resonance peak reduction, similarly to traditional resistive or resonant shunts, with higher performance for one degree of freedom host structure [33]. However, they cannot produce a "notch" type response, as a lightly damped resonant shunt does by creating an antiresonance. They are then not as efficient as an adaptive resonant shunt in the case of a tonal excitation filtering.

Recently, a new shunt technique was proposed, by considering that the shunt effect of the host structure could be chosen equivalent to a force in phase with the velocity of the structure, to be equivalent to a damping force [34, 35, 36]. To create this, a constant (DC) voltage source is connected to the piezoelectric transducer through a pulse width modulation (PWM) circuit, with the duty cycle modulated synchronously with the structure oscillations. It is shown that increasing the DC voltage can lead to a complete resonance peak cancellation, with possible unstabilities if the DC voltage is too large. To our knowledge, these contributions are the only one using PWM techniques for structural vibration reduction. Though using PWM circuits, our present contribution is based on a different point of view, since it is used to modulate the value of a given component of the shunt and not to fully synthetize a suitable shunt voltage signal.

A different approach, more related to active control, consists in using a feedback of a measurement of either displacement, velocity or acceleration, which is amplified to supply a magnetic or a piezoelectric transducer. It enables to change the apparent stiffness/inertia of the structure and thus its natural frequencies. Only a few recent references are given here. In [37], the principle is applied to a single degree of freedom oscillator with an acceleration feedback, to provide a tunable inertia effect to change the resonance frequency. In [38], a similar approach, with displacement feedback, is applied to a multi degree of freedom system (a clamped free piezoelectric beam), with

unconditional stability. In [39], the vibration damping of a plate is addressed by coupling it to a mechanical resonator enhanced with an inerter (a flywheel) and combined with an electromagnetic actuator and a velocity feedback, with stability issues due to a non colocalized control. In all these approaches, and contrary to the shunt and SSD techniques discussed above and addressed in the present paper, a power is injected in the system, which can lead to stability issues.

In the context of resonant shunts, the present article proposes an original technique to tune the electrical natural frequency of the shunt by using a PWM circuit. It is here realized with an electromagnetic transduction, but it could equally be realized with a piezoelectric transduction. Indeed, we use the PWM circuit to modulate the value of the capacitance of the shunt. It is shown that the electrical natural frequency is directly proportional to the duty cycle of the PWM, thus enabling an efficient and easy mean of tuning the resonant shunt in real time. As it will be shown, as compared to other works of the literature, our strategy has the advantage of being semi-passive (contrary to active control strategies, no energy is injected in the circuit so that the system dynamics is unconditionally stable. Only a small amount of energy is here necessary to supply the PWM circuit switches and their command). It is thus completely equivalent to a passive RC resonant shunt for which the value of C can be changed in real time. It shares similarities with the SSD family of techniques because we include switches in the shunt circuit. However, in our case, the switching (PWM) frequency is chosen much higher than the dynamics of the mechanical system, whereas in the SSD techniques, the switching is synchronized to the oscillations of the system and thus in the same frequency range. Whereas the SSD techniques are nonlinear (the switch commutation creates non-smooth oscillations and shocks), our technique is fully linear because of the separation of the frequency bands (the dynamics of the system and the PWM frequency).

The outline of the papers follows. Section 2 gives the basics of the PWM technique, showing that the low frequency dynamics of the system can be obtained by an average of its fast dynamics, at the PWM frequency. Section 3 presents a multi-mode model of an elastic structure coupled to the tunable resonant shunt. Then, section 4 shows an experimental validation of the PWM electronic circuits. Finally, section 5 presents an experimental validation of the tunable resonant shunt on a mechanical multi-mode elastic structure.

2. Pulse-Width Modulation theory

The basic component used in this article to obtain a tunable circuit is a chopper, that is placed between two electrical circuits Z_1 and Z_2. As shown in Fig. 1, it is composed of two switches A and B that are controlled by complementary periodic rectangular pulse signals to obtain a pulse-width modulation (PWM). If the PWM frequency $f_{\mathrm{PWM}} = 1/T$ (with T the period of the rectangular pulse signals) is chosen much larger with respect to the characteristic frequency content of the circuits Z_1 and Z_2, in average, circuits Z_1 is connected to Z_2 on a fraction of time only, that depends on the duty cycle β. Because
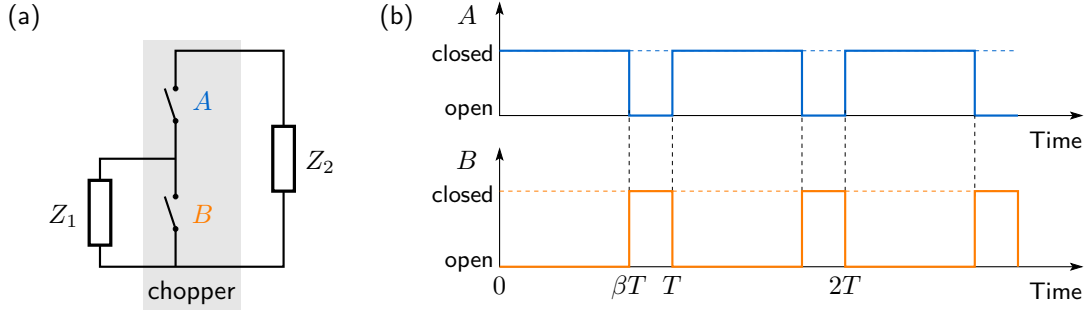
Figure 1. Chopper with pulse-width modulation of the two switches. (a) chopper circuit showing the two switches; (b) command of the two switches at period T with duty cycle β. $\beta = 0.75$ on the plots.

of this, the circuit behaves as if the characteristics of Z_2 were modulated, as a function of β.

Precisely, we consider a given period of the PWM command signals (for instance the first one, $t \in [0, T]$), as shown in Fig. 1(b). In the first part of the period, of duration βT, switch A is closed and switch B is open: circuit Z_1 and Z_2 are connected. In the second part of the period, of duration $(1 - \beta)T$, switch A is open and switch B is closed: Z_1 is short-circuited and doesn't "see" circuit Z_2. Consequently, in average, the whole dynamics of the circuit is equivalent to Z_1 connected to Z_2 for a fraction β of the time, whereas for the remaning $(1 - \beta)$ fraction of the time, it is equivalent to Z_1 only. The consequences of these basic properties are investigated on several circuits in the remaining of the section.

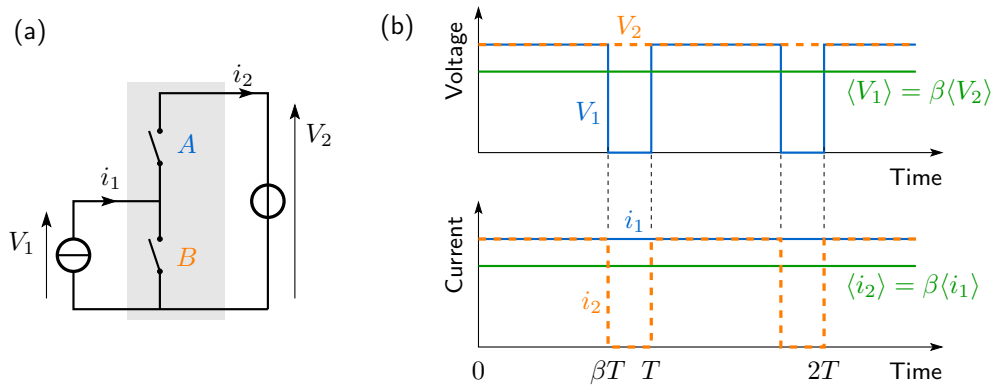### 2.1. Input / output relation with ideal current and voltage source

Figure 2. Chopper with ideal current and voltage sources. (a) Circuit; (b) time evolution of the voltages, currents and their average value as a function of duty cycle β. $\beta = 0.75$ on the plots.

A first insight in the PWM behaviour is investigated by considering the circuit of Fig. 1 with an ideal current source for circuit Z_1 and an ideal voltage source for circuit

Z_2, as shown in Fig. 2. The voltage / current pairs of circuit Z_1 and Z_2 are respectively denoted by (V_1, i_1) and (V_2, i_2). During the $(n + 1)$-th period $(n \in \mathbb{N})$, the state of the system is:

$$
\begin{cases}
V_1 = V_2, \quad i_2 = i_1, & \forall t \in [0, \beta T] + nT, \\
V_1 = 0, \quad i_2 = 0, & \forall t \in [\beta T, T] + nT.
\end{cases}
\tag{1a, 1b}
$$

In the first phase, switch A is closed and B is open, whereas in the second phase, switch A is open and B is closed. By defining the average of a variable $\bullet(t)$ over a period T by:

$$
\langle \bullet \rangle = \frac{1}{T} \int_t^{t+T} \bullet(\tau) \, \mathrm{d}\tau,
\tag{2}
$$

and using Eqs. (1), one obtains the following averaged relations:

$$
\langle V_1 \rangle = \beta \langle V_2 \rangle, \quad \langle i_2 \rangle = \beta \langle i_1 \rangle.
\tag{3}
$$

The above relations illustrate the effect of the PWM: in average, the two circuits on the left and the right of the chopper are connected to each other only a fraction β of the time. As a consequence, it appears that changing the value of the duty cycle β enables to change the average impedance of the circuit. Relations (3) are valid only with ideal voltage / current sources, which means that i_1 and V_2 must be constant. In other cases, as shown in §2.3, Eqs. (3) could be erroneous.

2.2. Dynamical model

To extend relations (3) to more complex electrical circuits, we consider that the chopper connects two circuits Z_1 and Z_2, as shown in Fig. 1, that are considered linear. Their dynamics is characterized by the state vector $\boldsymbol{x}(t)$. We denote by t_n the beginning time of the $(n + 1)$-th period and $\hat{t}_n = t_n + \beta T$ the switch time of the $(n + 1)$-th period. The PWM imposes to the system to switch between two successive configurations. Its dynamics can then be written in the state space as:

$$
\begin{cases}
\dot{\boldsymbol{x}} = \boldsymbol{A}_1 \boldsymbol{x} + \boldsymbol{b}_1 f, & \forall t \in [t_n \ \hat{t}_n], \\
\dot{\boldsymbol{x}} = \boldsymbol{A}_2 \boldsymbol{x} + \boldsymbol{b}_2 f, & \forall t \in [\hat{t}_n \ t_{n+1}],
\end{cases}
\tag{4a, 4b}
$$

where $\boldsymbol{A}_1$, $\boldsymbol{A}_2$ are the state matrices of the system in its two configurations, $\boldsymbol{b}_1$, $\boldsymbol{b}_2$ are two command vectors and $f(t)$ a driving function.

By considering that the PWM frequency $f_{\mathrm{PWM}} = 1/T$ is much larger than the characteristic frequencies of the system, namely the frequencies of the spectrums of $\boldsymbol{A}_1$ and $\boldsymbol{A}_2$ and of $f(t)$, it is possible to show that (see Appendix A for the mathematical details):

$$
\dot{\boldsymbol{x}}(t) \simeq \bar{\boldsymbol{A}} \boldsymbol{x}(t) + \bar{\boldsymbol{b}} f(t),
\tag{5}
$$

where

$$
\bar{\boldsymbol{A}} = \beta \boldsymbol{A}_1 + (1 - \beta) \boldsymbol{A}_2, \quad \bar{\boldsymbol{b}} = \beta \boldsymbol{b}_1 + (1 - \beta) \boldsymbol{b}_2.
\tag{6}
$$

As a consequence, if the PWM is fast enough with respect to the dynamics of the system, the latter is equivalent to a first order linear state space system whose dynamics is the average $(\bar{A}, \bar{b})$ of the two system characteristics (A_1, b_1) and (A_2, b_2), weighted by the duty cycle β, as shown by Eqs. (6). In particular, if $\beta \to 1$, the state of the system tends toward configuration 1, whereas if $\beta \to 0$, it tends toward configuration 2. If $\beta \in [0, 1]$, all intermediate states are possible.

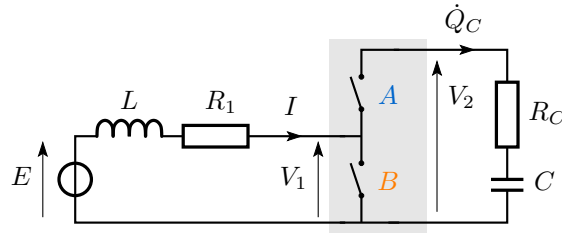## 2.3. A resonant electrical circuit with tunable capacitance

Figure 3. A RLC circuit with variable capacitance

To illustrate the results of the previous sections and introduce the resonant shunt, we consider the resonant electrical circuit of Fig. 3 with the switch command laws of Fig. 1(b). It is composed of a voltage source $E(t)$, an inductance L, a resistance R_1 in series, connected through a chopper to a capacitance C and a resistance R_C in series. This section is devoted to show that the chopper with a PWM enables to tune the value of the capacitor and thus of the resonance frequency of the circuit.

For the first phase of the PWM, switch A is closed, switch B is open, the two parts of the circuits are in series and the dynamics can be written:

$$\begin{cases} L\dot{I} + (R_1 + R_C)I + Q_C/C = E, & \text{(7a)} \\ \dot{Q}_C = I, & \text{(7b)} \end{cases}$$

where Q_C is the electric charge in the capacitor and I is the current intensity in the inductor. For the second phase of the PWM, switch A is open, switch B is closed, the left part of the circuit is short circuited and the right part is in open circuit. The dynamics thus reads:

$$\begin{cases} L\dot{I} + R_1 I = E, & \text{(8a)} \\ \dot{Q}_C = 0. & \text{(8b)} \end{cases}$$

By defining the state vector as $x = [I \ Q_C]^{\mathrm{T}}$, this gives the following state matrices and command vectors (defined in Eq. (4)) for the two configurations of the present circuit:

$$A_1 = \begin{pmatrix} -\frac{R_1+R_C}{L} & -\frac{1}{LC} \\ 1 & 0 \end{pmatrix}, \quad A_2 = \begin{pmatrix} -\frac{R_1}{L} & 0 \\ 0 & 0 \end{pmatrix}, \quad b_1 = b_2 = \begin{pmatrix} \frac{E}{L} \\ 0 \end{pmatrix}. \tag{9}$$

Consequently, following Eq. (6), the averaged dynamics is defined by:

$$\bar{A} = \begin{pmatrix} -\frac{R_1 + \beta R_C}{L} & -\frac{\beta}{LC} \\ \beta & 0 \end{pmatrix}, \quad \bar{b} = \begin{pmatrix} \frac{E}{L} \\ 0 \end{pmatrix}, \tag{10}$$

which gives:

$$\begin{cases} L\dot{I} + (R_1 + \beta R_C)I + \beta Q_C/C = E, & \text{(11a)} \\ \dot{Q}_C = \beta I. & \text{(11b)} \end{cases}$$

Finally, by defining the charge Q as $\dot{Q} = I$, integrating Eq. (11b) and assuming that the charge in the capacitor is zero at $t = 0$, one obtains $Q_c = \beta Q$ and:

$$L\ddot{Q} + R(\beta)\dot{Q} + \beta^2 Q/C = E, \tag{12}$$

for the averaged (slow) dynamics of the circuit, with $R(\beta) = R_1 + \beta R_C$. It is then equivalent to a resonant circuit (if R is small enough), with an equivalent capacitance C/β^2, that can be modified by adjusting the value of the duty cycle β. The direct consequence of the PWM is that the apparent natural frequency of the circuit is now:

$$\bar{\omega}_e = \beta \omega_e = \frac{\beta}{\sqrt{LC}}. \tag{13}$$

It is then shown that the PWM is a mean of adjusting the resonance frequency of a resonant electrical circuit and that it is proportional to the duty cycle β.

An indirect consequence of the PWM appears if a resistance R_c is present in series with the capacitor (in practice, it can be the equivalent series resistance of the capacitor): its apparent value is βR_c, which depends on the duty cycle, thus meaning that the total resistance R of the circuit is modified by the PWM.

Another remark is that Eqs. (11) (or (12)) cannot be obtained with relations (3), which are valid for constant only current / voltage sources in the circuit of Fig. 2. Here, the current intensity $I(t)$ in the left part of the circuit of Fig. 3 can be considered constant at the characteristic time of the PWM, since it is a continuous function of time (its dynamics is governed by the two equations (7a) and (8a)). The left part of the circuit can then be approximated by a constant current source $i_1 = I$. On the contrary, the voltage in the right part of the circuit is not constant. In fact, $V_2(t) = R_C\dot{Q}_C + Q_C/C$, with $i_2 = \dot{Q}_C$ which is a rectangular pulse signal. Consequently, $V_2(t)$ cannot be considered as a DC voltage source, $\langle V_1 \rangle \neq \beta \langle V_2 \rangle$, which invalidates the first equation (3). Notice that all the other equations are valid: $\langle i_2 \rangle = \beta \langle i_1 \rangle$ (it is Eq. (11b)) as well as Eqs. (1) (Eqs. (7) and (8)). As a conclusion, one is forced to use Eqs. (6) instead of Eqs. (3) to write the averaged dynamics of the circuit with PWM.

Finally, it is interesting to consider the electrical admittance of the circuit, which reads:

$$Y_0(\Omega) = \frac{j\Omega\hat{Q}}{\hat{E}} = \frac{j\Omega}{\beta^2/C - L\Omega^2 + jR\Omega}, \tag{14}$$

where $\hat{\bullet}(\Omega)$ is the Fourier transforms of $\bullet(t)$ and $j = \sqrt{-1}$. A useful property of this admittance is that the amplitude resonance occurs exactly at $\Omega = \bar{\omega}_e$, with a corresponding admittance value of

$$Y_{\max} = Y(\bar{\omega}_e) = 1/R. \tag{15}$$

Consequently, the total resistance of the resonant circuit can be easily estimated by the inverse of the maximum of the admittance plot. This will be illustrated in section 3.2 and Fig. 5.
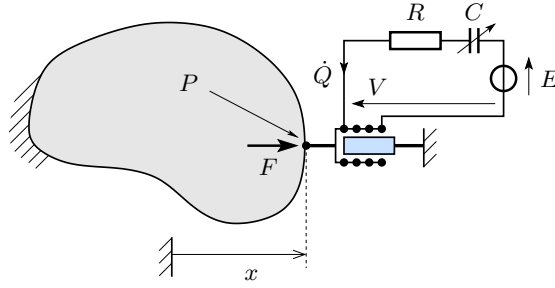
3. Model for the tunable resonant shunt

Figure 4. Principle of a tunable resonant shunt connected to an elastic mechanical structure

3.1. Governing equations

In this section, we address the coupling of the tunable resonant electrical circuit of Fig. 3 to a mechanical structure, through an electromagnetic transducer, as depicted on Fig. 4. We gather the displacements of all the points of the structure in a vector $\boldsymbol{u}(t)$, which is expanded on a subset of $N \in \mathbb{N}^*$ modes $(\omega_i, \boldsymbol{\Phi}_i)$, $i = 1, \ldots N$, of the natural mode basis of the structure with the electromagnetic transducer in open-circuit:

$$\boldsymbol{u}(t) = \sum_{i=1}^{N} \boldsymbol{\Phi}_i x_i(t), \tag{16}$$

where $x_i(t)$ is the i-th modal coordinate. One obtains the following set of equations [9]:

$$\begin{cases} m_i \ddot{x}_i + c_i \dot{x}_i + k_i x_i + \phi \dot{Q} = F_i, & \text{(17a)} \\ L\ddot{Q} + R(\beta)\dot{Q} + \beta^2 Q/C - \phi \sum_{i=1}^{N} \dot{x}_i = E, & \text{(17b)} \end{cases}$$

where m_i, c_i, k_i are the modal mass, damping constant and stiffness of the i-th mode, F_i is the mechanical i-th modal excitation, L is the inductance of the EM transducer

and ϕ its force factor (of units N/A or V/(m/s)). The tunable capacitance of the shunt is C/β^2 and its resistance R. This latter parameter is the equivalent resistance of the circuit, that can be written $R(\beta) = R_1 + R_n + \beta R_C$: it gathers the resistance R_1 of the EM transducer, the one of the capacitor R_C, as explained in section 2.3, and an additional one R_n that can be tuned experimentally to adjust the value of R. We will see in section 5 that R_n has to be negative to optimally tune the shunt, because R_1 is in practice too large. Finally, a voltage source $E(t)$ was included in the circuit, for experimental purpose, as it will be seen in section 5.

At this step, it is convenient to introduce the following parameters: the mechanical natural frequencies ω_i of the mechanical system, the modal damping factors ξ_i, the modal electromechanical coupling factors κ_i and the electrical damping factor ξ_e, by:

$$\omega_i = \sqrt{\frac{k_i}{m_i}}, \quad \xi_i = \frac{c_i}{2\sqrt{k_i m_i}}, \quad \kappa_i = \frac{\phi}{\omega_i \sqrt{m_i L}}, \quad \xi_e = \frac{R_1/\beta + R_C}{2}\sqrt{\frac{C}{L}}. \quad (18)$$

As explained in the introduction section 1, two complementary strategies can be used with the resonant shunt to reduce the vibrations of the mechanical structure. The first one consists in tuning the electrical natural frequency $\bar{\omega}_e$ close to a mechanical frequency ω_i and to adjust the electrical damping ratio to cut as much as possible the resonance peak. The theoretical optimal tuning of the parameters is, with a one mode model ($N = 1$ in Eq. (16), see [9] and reference therein):

$$\omega_e^{\text{opt}} = \omega_i \sqrt{\frac{2 - \kappa_i^2}{2}}, \quad \xi_e^{\text{opt}} = \sqrt{\frac{3\kappa_i^2}{4(2 - \kappa_i^2)}}. \quad (19)$$

For a multi-mode situation, the tuning is not as straightforward, as investigated in [40]. This strategy is efficient as long as the damping factor ξ_i of the considered mode is small and the electromechanical coupling factor κ_i is large. It is also very interesting for a broadband excitation signal since it enables to reduce the amplitude of the resonance peak without adding the two side resonances [9]. This case will be experimentally investigated in section 5.4.

3.2. A tunable antiresonance shunt

In the case of a harmonic excitation of known frequency Ω ($F_i(t) = F_{i0} \cos \Omega t$ in Eq. (17a)), it is possible to use the tunable resonant shunt in a more efficient way. This second strategy consists in having the resonant shunt as less damped as possible, in order to create an antiresonance. Since it is tunable, it is then possible to adjust the duty cycle β to tune the antiresonance frequency close to Ω, to take the benefit of the antiresonance. To theoretically explain this strategy, we consider the displacement $x(t)$ of the structure at point P, at which the electromagnetic transducer is connected (see Fig. 4). We also choose the scaling of the mode shapes $\mathbf{\Phi}_i$ such that their component associated to the displacement of point P is one. It is always possible for all modes with a non zero modal component at point P. Consequently, modes uncoupled to the
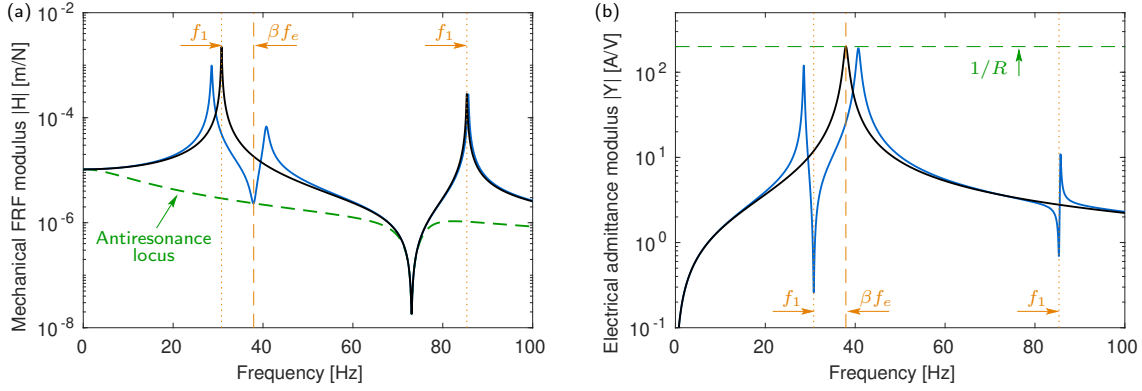
Figure 5. Theoretical frequency response of the mechanical structure coupled to a tunable resonant shunt with the identified parameters of section 5.2 and $N = 2$ mechanical modes. (a) Modulus of the collocated mechanical frequency response $H(\Omega) = \hat{x}/\hat{F}$ at the connection point of the electromagnetic transducer as a function of excitation frequency $f_{\mathrm{exc}} = \Omega/(2\pi)$. The locus of the electrical antiresonance, at $f_{\mathrm{exc}} = \beta f_e = \beta \omega_e/(2\pi)$, when β is varied, is also shown; (b) modulus of the electrical admittance $Y(\Omega) = j\Omega\hat{Q}/\hat{E}$ as a function of f_{exc}. The maximum $Y_{\max} = 1/R$ is also shown. The black curves correspond to the system's response without electromechanical coupling (*i.e.* with $\phi = 0$). $f_1 = \omega_1/(2\pi)$ and $f_2 = \omega_2/(2\pi)$ are the natural frequencies of the mechanical system. In this plot, $\beta = 0.43$ and $R = 5$ mΩ.

EM transducer are implicitly not retained in the modal expansion of Eq. (16). One can then write:

$$x(t) = \sum_{i=1}^{N} x_i(t). \tag{20}$$

We also consider that the forcing is reduced to a single point force $F(t)$ applied at point P (see Fig. 4). In this case, with the scaling of the mode shapes, $F_i(t) = F(t) \ \forall i = 1, \ldots N$. If we denote by a hat the Fourier transforms ($\hat{\bullet}(\Omega)$ is the Fourier transforms of $\bullet(t)$), the governing equations (17) in the frequency domain reads :

$$\begin{pmatrix} Z_{10}(\Omega) & \cdots & 0 & j\Omega\phi \\ \vdots & \ddots & \vdots & \vdots \\ 0 & \cdots & Z_{N0}(\Omega) & j\Omega\phi \\ -j\Omega\phi & \cdots & -j\Omega\phi & Z_{e0}(\Omega) \end{pmatrix} \begin{pmatrix} \hat{x}_1 \\ \vdots \\ \hat{x}_N \\ \hat{Q} \end{pmatrix} = \begin{pmatrix} \hat{F} \\ \vdots \\ \hat{F} \\ \hat{E} \end{pmatrix} \tag{21}$$

where, for all $i = 1, \ldots N$:

$$Z_{i0}(\Omega) = k_i - m_i\Omega^2 + jc_i\Omega, \quad Z_{e0}(\Omega) = \beta^2/C - L\Omega^2 + jR\Omega, \tag{22}$$

are the modal and electrical impedances of the system without electromechanical coupling ($\phi = 0$). With $E(t) = 0$ in the above equation, solving the linear system leads to the following mechanical modal frequency response functions:

$$H_i(\Omega) = \frac{\hat{x}_i(\Omega)}{F_0} = L\left(\bar{\omega}_e^2 - \Omega^2 + 2j\xi_e\bar{\omega}_e\Omega\right) \prod_{\substack{n=1 \\ n\neq i}}^{N} m_n\left(\omega_n^2 - \Omega^2 + 2j\xi_n\omega_n\Omega\right) \Big/ D(\Omega), \tag{23}$$

where $j = \sqrt{-1}$ and $D(\Omega)$ is the determinant of the main matrix of Eq. (21). It is not given here for a sake of conciseness.

The main consequence of Eq. (23) is its antiresonance property, because of the first term, which is present in the numerator of any $\hat{x}_i$: if the electrical system is conservative, i.e. $\xi_e = 0$, the first term is zero and then, all modal coordinates $\hat{x}_i$ are zero for $\Omega = \omega_e$. Consequently, if $\Omega = \omega_e$, Eq. (16) shows that the displacement vector $\boldsymbol{u}(t)$ is strictly zero in the steady state, which means that the structure remains at rest. In this case, the electrical force created by the shunt exactly compensates $F(t)$.

If $\xi_e \neq 0$ but remains small, the frequency response function of any point of the structure presents a minimum at $\Omega \simeq \bar{\omega}_e$, which goes deeper as the damping get smaller. This is illustrated in Fig. 5(a), in which the antiresonance is clearly noticeable at $\Omega \simeq \bar{\omega}_e = \beta \omega_e$. This figure also shows the locus of the antiresonance point when the duty factor β (and thus the electrical frequency $\bar{\omega}_e = \beta \omega_e$) is varied. It appears that in the particular case of a harmonic excitation at frequency Ω, if the electrical frequency is tuned such that $\bar{\omega}_e = \Omega$, the mechanical response of the structure in the steady state is given by the green dashed curve of Fig. 5(a). This curve shows the efficiency of the method, since the two mechanical resonances have completely disappeared.

The above described property of an antiresonance *for all points of the system and strictly at* $\Omega = \bar{\omega}_e$ ceases to exist in two conditions. The first one is if the forcing is not collacated with the electromechanical transducer, i.e. if it is applied at another point than P. In this case, different modal forcings appear in the second member of Eq. (23) and the property is lost. There are still antiresonances, which are close to $\Omega = \bar{\omega}_e$ and which depend on the considered point on the structure. A second condition appears if the electromagnetic transducer right terminal on Fig. 4 is not perfectly connected to the ground. In this case, some energy can be transfered to modes of the structure that are not excited by $F(t)$. A zero would then appear, instead of $\hat{F}$, in the corresponding line of the second member of Eq. (21). This would completely break the antiresonance property.

Another concern is the electrical admittance of the shunt, namely $Y(\Omega) = j\Omega \hat{Q}/\hat{E}$, where $E(t)$ is an direct voltage source in the electrical circuit. Using Eq. (21), one can show that:

$$Y(\Omega) = j\Omega \prod_{n=1}^{N} m_n \left(\omega_n^2 - \Omega^2 + 2j\xi_n \omega_n \Omega \right) \Big/ D(\Omega). \qquad (24)$$

With no electromechanical coupling ($\phi = 0$), $Y(\Omega) = Y_0(\Omega)$: it is equal to the admittance of the electrical circuit, which displays a resonance at $\Omega = \bar{\omega}_e$. With $\phi \neq 0$, as shown in Fig. (5), the admittance plot is modified by the mechanical resonances and shows antiresonances close to the mechanical natural frequencies, at $\Omega = \omega_i$, $i = 1, \ldots N$. Moreover, the property described at the end of section 2.3 is not strictly verified, but is closed to: the maximum of the admittance plot is very close to $1/R$, which gives a mean of estimating the total electrical resistance R.

4. Experimental validations on electrical circuits

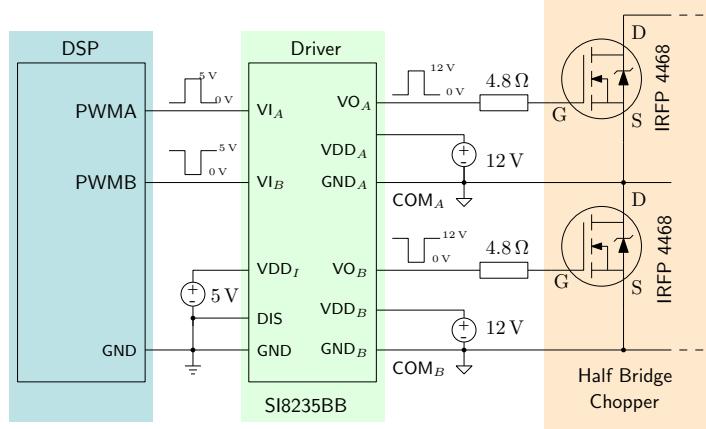### 4.1. Practical implementation of the chopper

Figure 6. Schematic of the chopper

The schematic of electronic circuit and its practical implementation build for the experiments are depicted in Fig. 6. It essentially consists in an inverter leg realized using two MOSFETs (International Rectifier IRFP 4468Pbf) which were selected considering their low drain to source resistance (typically $2\,\mathrm{m\Omega}$) when switched on, their high switching frequency (up to $100\,\mathrm{kHz}$) and their maximum voltage rating ($100\,\mathrm{V}$). Since the current changes of sign during operation, the switches must be bidirectional which is ensured by the built in diode of the component. The gates are connected to the driver through gate resistors to limit the peak gate current at *ca.* $2.5\,\mathrm{A}$. The driver (Silicon Labs SI8235BB) isolates the Digital Signal Processor (DSP) on one side from the power side providing floating grounds GND_A and GND_B. Therefore, two isolated power supplies (Murata CMD0512bE) generate two independent $12\,\mathrm{V}$ supplies (VDD_A and VDD_B) from VDD_I. The driver replicates and amplifies the PWMA and PWMB control signals ($0\,\mathrm{V}$ to $5\,\mathrm{V}$) to realize the gate drive signals VO_A and VO_B ($0\,\mathrm{V}$ to $12\,\mathrm{V}$), and it is able to supply up to $4\,\mathrm{A}$ peak current. The gate resistors values chosen here ensure a fast switching of the MOSFETs. The PWM signals are provided, according to the experiments by an Arduino (§4.2) or by dedicated peripherals of a dSpace 1104 (§4.3, §5). As the driver does not provide deadtime control to protect the switches from through short-circuits, they were directly programmed in the DSP. Finally, the SI8235BB provides an inhibition input (DIS) which was driven to low enabling unconditionnaly the PWM.

4.2. Effective duty cycle

To validate the behaviour of the chopper introduced in the previous section 4.1, we consider the circuit of Fig. 7. It is composed of the chopper of Fig. 6, with a DC voltage
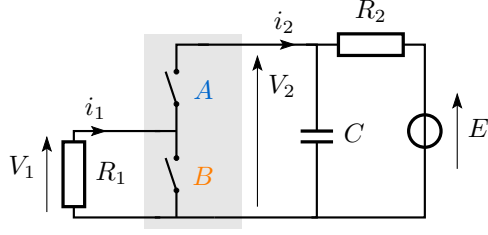
Figure 7. Circuit used for the validation of the input / output rule of the chopper.

source E. In practice, E is realized by a laboratory voltage supply that has to be protected from the current ripples due to the PWM. We then add a resistor $R_2 = 1$ kΩ and a capacitor $C = 1$ μF to create a low pass filter to filter them. A load resistor $R_1 = 1525$ Ω is used to measure $V_1(t)$. The PWM frequency is $f_{\mathrm{PWM}} = 31.25$ kHz, giving a PWM period of $T = 1/f_{\mathrm{PWM}} = 32$ μs.
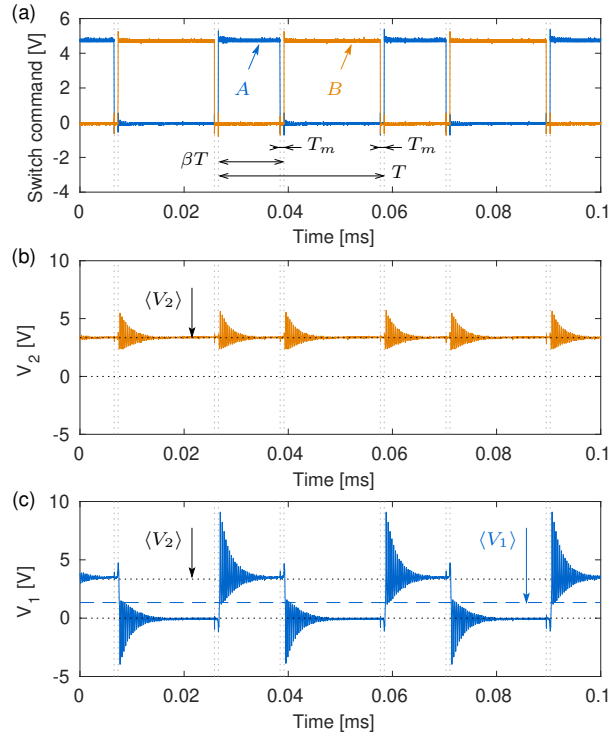

Figure 8. (a) Time evolution of the command signals of switch A and B; (b,c) time evolution of voltage $V_1(t)$ and $V_2(t)$. Their average values $\langle V_1 \rangle$ and $\langle V_2 \rangle$ are also shown. The duty cycle is $\beta = 0.375$.

Because in practice the switch time in the MOSFETs is not instantaneous, the theoretical command laws of Fig. 1 are applied with deadtimes: at each change of the switch states, a short time with both switches open is programmed. Fig. 8(a) shows the experimental time evolution of the switch command signals. With a command signal of 0 V, the switch is open and with $\simeq 4$ V, the switch is closed. Deadtimes of duration

T_m are clearly visible. In this situation, the effective time in which the circuit is in configuration 1 is reduced as compared to the theoretical PWM of Fig. 1: instead of being βT, it is $\beta T - T_m$. As a consequence, the effective duty cycle is in practice:
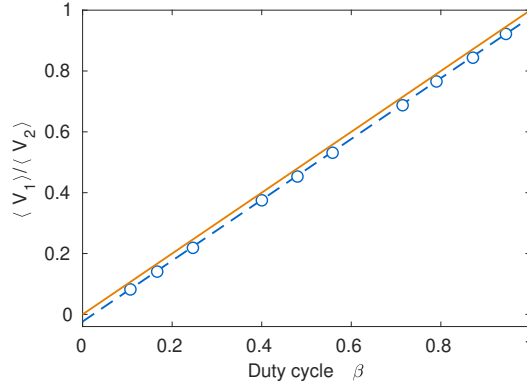
$$\beta_{\text{eff}} = \beta - T_m/T. \tag{25}$$

Figure 9. 'o': Ratio $\langle V_1 \rangle / \langle V_2 \rangle$ of the average values of V_1 and V_2, for several values of the duty cycle β, with the circuit of Fig. 7; '—' curve $y = \beta$; '- -': curve $y = \beta - T_m/T$ (Eq. (25)).

To illustrate and verify this behaviour, Fig. 8(b,c) show the time evolution of voltages $V_1(t)$ and $V_2(t)$ and their average values. It is observed that some high frequency damped oscillations appear each time one of the switches is closed, due to parasitic inductor and capacitor in the circuit. Since those oscillations are at high frequency, higher that the PWM frequency, they have no effect on the low frequency averaged dynamics of the system. Then, we computed the average values $\langle V_1 \rangle$ and $\langle V_2 \rangle$ of $V_1(t)$ and $V_2(t)$ over a number of periods and repeated the operation for several values of the duty cycle β. In theory, the present circuit behaves like the one investigated in section 2.1 and one should observe $\langle V_1 \rangle = \beta_{\text{eff}} \langle V_2 \rangle$, with the effective duty cycle β_{eff} defined by Eq. (25). To verify this, the ratio $\langle V_1 \rangle / \langle V_2 \rangle$ is plotted as a function of β in Fig. 9. It is observed that the law (25) is perfectly verified, thus validating our PWM model. In the present case, the deadtime was chosen such that $T_m = 0.0235T$.

4.3. A resonant circuit with variable capacitance and negative resistance

This section is devoted to the experimental realization of the tunable resonant electrical circuit of section 2.3 (Fig. 3). If the inductance L is realized in practice with a standard coil, its internal resistance R_L is often large. Because we want to observe a resonant response with a sharp peak, we have to reduce this resistance. This is done in practice by adding in the circuit a negative resistance R_n, realized here with a real time digital signal processor (DSP) (it is also possible to use an analog circuit built with operational amplifier, see for instance [9]). This DSP will also be used to create the command signals of the chopper switches.
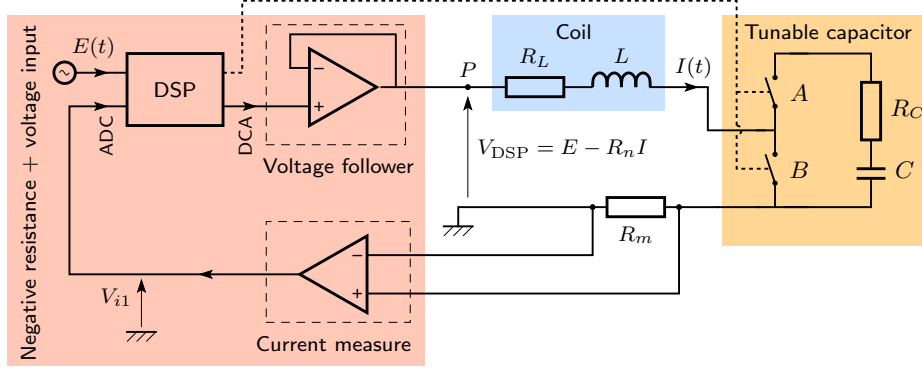
Figure 10. Practicle tunable RLC circuit with a negative resistance.

The practical realization of this circuit is shown in Fig. 10 and 13(d). The coil is modelled by an inductance L and a resistance R_L (blue shaded area of Fig. 10). The capacitor of capacitance C and internal resistance R_C is connected to the circuit through the chopper of sections 4.1 and 4.2, with a PWM command of duty cycle β (orange shaded area of Fig. 10). This command of the chopper is realized by the DSP, which is here a dSpace CP1104, which is also used to synthesized the negative capacitance (pink shaded area of Fig. 10). For this, the DSP is programmed to create a voltage output V_{DSP} which is proportional to the current $I(t)$ in the coil, with a negative coefficient: $V_{\mathrm{DSP}} = -R_n I$, with $R_n > 0$ the absolute value of the negative resistance. In practice, a measuring current circuit is used, built with a current sense amplifier (INA 240A4, Texas instrument), with enhanced PWM rejection which provides increased attenuation of large common-mode transients. A very low measuring resistance $R_m \simeq 20\,\mathrm{m\Omega}$ is used, to minimize the electrical damping added in the circuit. As seen in the following, R_m is very small compared to the resistance of the circuit, $R_L \simeq 1\,\Omega$. A voltage $V_{i1} = R_m I(t)$ is then sent to the DSP. Since the INA240A4 has a 200 V/V built in amplification and the measurement shunt is *ca.* $R_m = 20\,\mathrm{m\Omega}$, the current gain is 4.1 V/A for this set-up. Finally, the output voltage signal created by the DSP is sent to a voltage follower, connected at the input point P of the circuit, so that the pink shaded circuit of Fig. 10 is equivalent to a voltage source V_{DSP} between point P and the ground.

The DSP is also used to deliver the excitation electrical signal $E(t)$ in the circuit, for the measurements of the electric admittance $Y(\Omega)$. In practice, this signal, of the form of a periodic chirp, is synthesized by a dynamic signal analyzer hardware (A VibPilot hardware of m+p international), also used to record and to make all the frequency analyzes of the signals. $E(t)$ is then sent to an input of the DSP, which is programmed to synthetize and output signal of the form $V_{\mathrm{DSP}}(t) = E(t) - R_n I(t)$.

As a consequence, the theory of section 2.3 shows that the averaged (slow) dynamical behaviour of the circuit is given by Eq. (12), with

$$R(\beta) = R_L + R_m - R_n + \beta R_C \tag{26}$$

and $\dot{Q} = I(t)$. The value of R_n can then be chosen to reduce and adjust the

total resistance R of the circuit. Moreover, it is possible to measure the admittance $Y(\Omega) = \hat{I}/\hat{E}$ of the circuit by measuring the signals $I(t)$ and $E(t)$, which are directly available in the DSP and which can be sent to the dynamic signal analyzer.
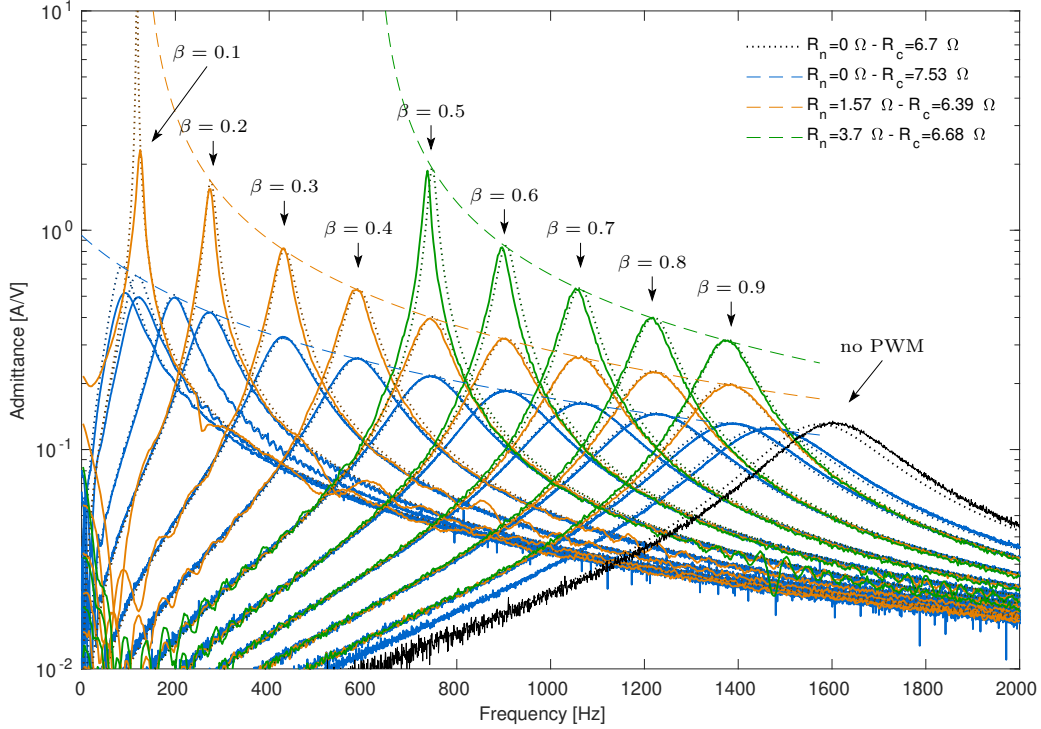

Figure 11. Admittance modulus of the RLC circuit for various values of the duty cycle β ($\beta \in \{0.1; 0.2; \ldots 0.9\}$) and the negative resistance R_n. Each value of R_n is associated to a particular color (blue for $R_n = 0$; orange for $R_n = -1.57\ \Omega$; green for $R_n = -3.7\ \Omega$). The black curves are associated to the circuit without the chopper. Both experiments and theoretical results are shown: '—': experiments; '···': model; '--': theoretical locus of admittance maxima.

We first measured the admittance $Y(\Omega)$ of the circuit without the chopper. Then, we measured it with the chopper, for various values of the duty cycle β and of the negative resistance R_n. The obtained admittances modulus are shown on Fig. 11. We can first qualitatively observe the effect of the duty cycle and of the negative resistance: increasing β leads to a decrease of the resonance frequency $\bar{\omega}_e$ of the admittance and increasing R_n leads to an increase of the resonance peak.

To compare the experiments with theory, Fig. 12(left) shows the experimental resonance frequencies, picked up on the admittance curves of Fig. 11, as a function of the effective duty cycle $\beta_{\text{eff}} = \beta - T_m/T$, with $T_m = 0.025T$. Considering theory, the resonance frequency is (see Eq. (13)) $\bar{\omega}_e = \beta_{\text{eff}}\omega_e$, with $\omega_e = 1/\sqrt{LC}$ the natural frequency of the circuit without the chopper. With the linear fit (with a zero y-intercept), we can observe that the experimental points are almost perfectly aligned, thus validating theory. Moreover, the slope of the linear fit gives an estimation value of $f_e = \omega_e/(2\pi) = 1574$ Hz, the natural frequency of the electrical circuit.
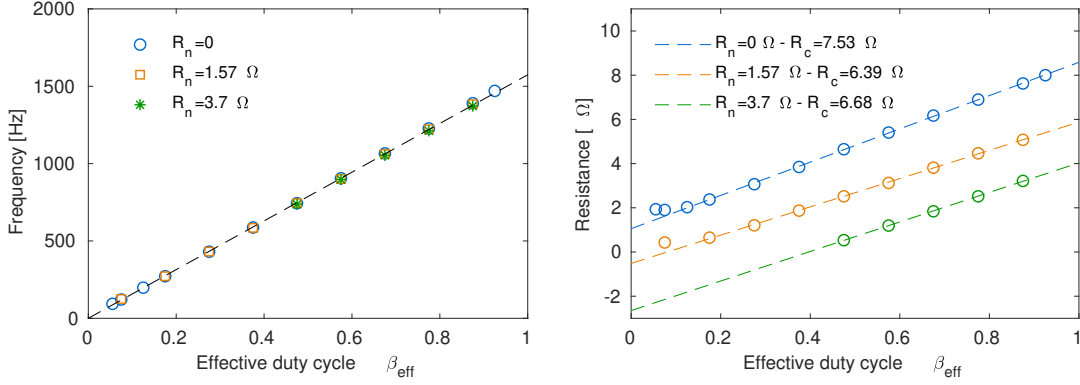
Figure 12. Resonance frequency $\bar{\omega}_e/(2\pi)$ (right) and total resistance R (left) as a function of the effective duty cycle β, for various values of the negative resistance R_n.

Then, Fig. 12(right) shows the equivalent resistance R as a function of the effective duty cycle β_{eff} and for the three values of the negative resistance R_n. Following theory, $R = 1/Y_{\text{max}}$ (Eq. 15), so that the values of Fig. 12(right) have been obtained with the inverse of the admittance modulus maxima, picked up on Fig. 11. Linear fits show an excellent agreement with theory that states $R = R_L + R_m - R_n + \beta R_C$ and enable to estimate the following values: $R_L = 1.05\ \Omega$, $R_n \in \{0; 1.57; 3.7\}\ \Omega$, $R_c \in \{7.53; 6.39; 6.68\}\ \Omega$ (we considered that $R_m = 20\ \text{m}\Omega \ll R_L$). One can remark that theory slightly fails to predict the correct resistive behaviour for low values of the duty cycle (namely $\beta < 0.2$), showing that in these cases, the PWM increases the losses above what is predicted by theory, based on a perfect PWM. One can also remark that the equivalent series resistance R_c of the capacitor is slightly modified by the PWM. This is probably due to the conduction losses in the MOSFETs diode, which turn on voltage is 1.3 V.

Based on the above estimated values and $L = 4.65\ \text{mH}$, $C = 2.20\ \mu\text{F}$ (estimated by fitting of the low and high frequency parts of the admittance plots and compatible with the manufacturer values of the components), theoretical admittance plots, using Eq. (14), are also shown on Fig. 11, showing an excellent agreement with the experiments. In particular, the theoretical curves that connect the admittance modulus maxima is also shown. Its equation is:

$$Y_{\text{max}} = \frac{1}{R_L + R_m - R_n + R_C\Omega/\omega_e},\tag{27}$$

stemming from Eqs. (26) and (15). Those plots also validate the low frequency approximation of the dynamics of the system, since the PWM frequency of $f_{\text{PWM}} = 20\ \text{kHz}$ is one order of magnitude larger than the frequency band $[0, 2000]$ Hz of interest.

One can notice a slight change in the electrical natural frequency f_e, between the cases with PWM ($f_e = 1574$ Hz, all dotted curves of Fig. 12) and without PWM ($f_e = 1600$ Hz, solid black curve). This can be probably explained by parasitic inductance and capacitance effects, due to the wires of the practical electronic implementation of

the chopper. In our model, we kept $C = 2.20\ \mu$F.

5. Experimental validation on a mechanical system

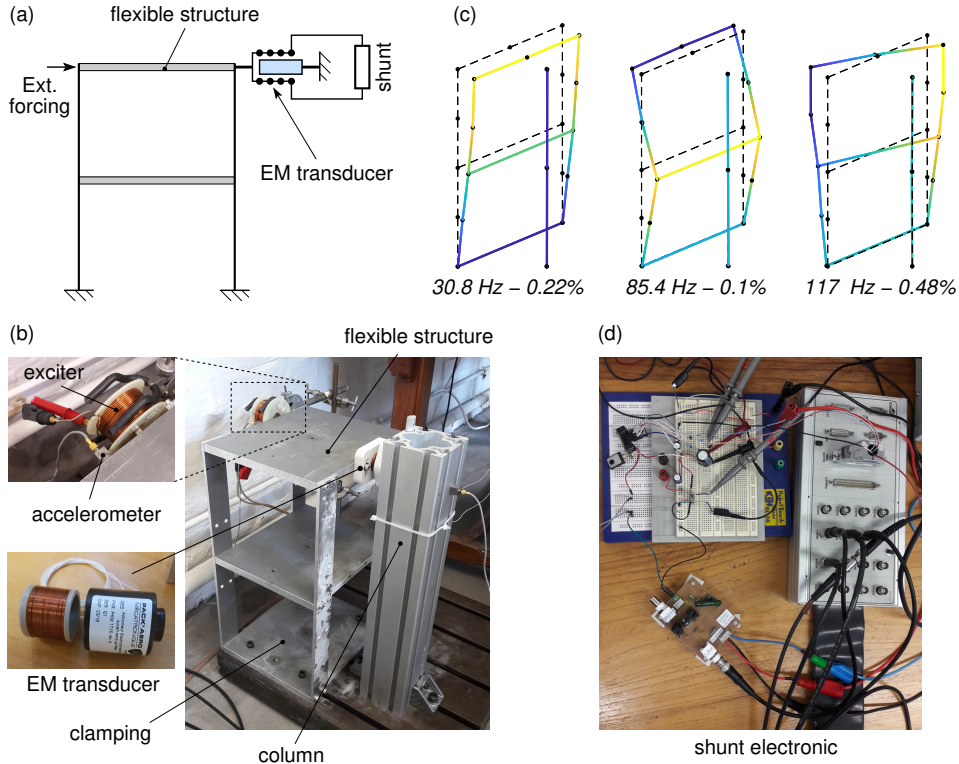### 5.1. Experimental setup

Figure 13. (a) Scheme and (b) picture of the structure under test, the EM transducer and the coil-magnet exciter; (c) first three mode shapes, measured with an accelerometer and an impact hammer; (d) electronic circuit for the shunt.

An experimental mechanical flexible structure, used previously in [9], shown in Fig. 13, was designed to test the tunable resonant shunt. It is composed of three identical plates, the bottom one being clamped to a frame, sustained by four identical beams, all built in aluminium. The geometrical characteristics were chosen to obtain two bending modes as the first two modes (with $f_1 = 30.8$ Hz and $f_2 = 85.4$ Hz their eigenfrequencies, see Fig. 13(c)), with the first twisting mode shifted to higher frequencies (at 117 Hz).

An electromagnetic transducer in the form of a voice coil (VCA, model PKM 1715, Pack Aero, France), shown in Fig. 13(b), enabled to couple the vibrations of the structure to the tunable resonant shunt electronic circuit (labelled "shunt" in Fig. 13(a)). It is composed of a coil in the form of a solenoid, fixed in the middle of the top plate of the structure, free to move in a radial magnetic field created by a permanent magnet clamped to the frame with a rigid column. To couple the vibrations of the structure

to the electromagnetic shunt, the terminals of the coils are connected to the electrical setup of Fig. 10, *i.e.* the coil of the VCA is the (L, R_L) blue shaded area.

It was verified that the fundamental vibration mode of the column was in the higher frequencies with respect to the frequency band of interest (around 187 Hz), not to disturb the behaviour of the system around its first two modes, between 0 and 120 Hz. Observing the modes shapes of the first two modes (Fig. 13(c)) also show that the oscillations of the column are negligible, proving that the motion of the column is uncoupled from the one of the flexible structure. This is mandatory, as explained at the end of section 3.2, if ones want to verify the antiresonance property.

The force factor of the VCA was estimated at $\phi = 2.98$ N/A. It was measured by sending a voltage signal $V(t)$ to the terminals of the coil and by measuring the mechanical velocity $v(t)$ between the coil and the magnet. A plateau in the modulus of the frequency response function $\hat{V}/\hat{v}$ led to the value of ϕ.

A coil magnet exciter (with a fixed coil and a small cylindrical magnet glued near the middle of the top plate, see Fig. 13(b)) was used to drive in vibrations the structure. It is identical to the one used in [41]. Measuring the current intensity signal $I_{dr}(t)$ in this coil, assumed proportional to the force F applied to the structure, gave a reference for the frequency response functions (FRF) measured in the experiments presented in this article. A calibration, with an impact hammer test, gave the following relation, used in the following for all the FRF plots: $F/I_{dr} = 0.133$ N/A. An accelerometer was glued in the middle of the top plate, in a direction aligned with the location of the EM transducer. Considering that the top plate remains rigid, this accelerometer was able to measure the acceleration $\gamma(t) = \ddot{x}(t)$ of the connection point of the EM transducer.
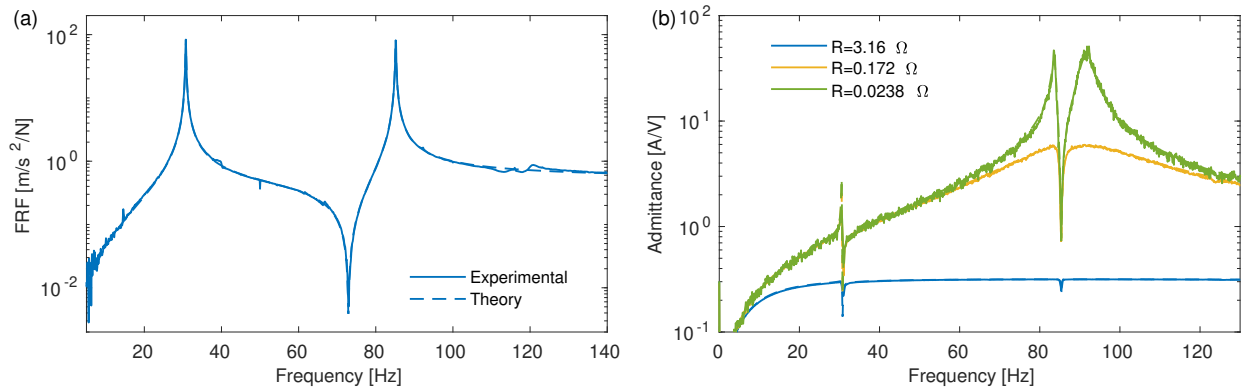
5.2. Model updating

Figure 14. Model updating. (a) Mechanical Frequency Response Function $H_\gamma(\Omega)$ with the EM transducer in open circuit; (b) Electrical Admittance $Y(\Omega)$ with no chopper for various negative resistances (the total resistance in the circuit is indicated in the legend); '—': experiments; '- -': updated theoretical model

	Natural frequency [Hz]	Damping ratio [%]	Modal mass [kg]
mode 1	30.77	0.22	2.72
mode 2	85.35	0.1	6.14

Table 1. Mechanical parameters estimated thanks to the FRF $H_\gamma(\Omega)$ of Fig. 14(a).

We identified all the parameters of the model of Eqs. (17) through dedicated experiments. We measured first the mechanical FRF $H_\gamma(\Omega) = \hat{\gamma}/\hat{F}$ (by imposing the force $F(t)$ with the coil/magnet driving system and measuring the accelerometer signal $\gamma(t)$) with the EM transducer in open circuit. Then, we estimated the values of the mechanical parameters, gathered in Tab. 1, using the model of Eqs. (17) with $\dot{Q} = 0$ and $N = 2$ modes retained in the modal basis. We obtained the plot of Fig. 14(a), showing a perfect agreement between the model and the experiments. One can notice that the torsion mode, with a natural frequency at 117 Hz, is uncoupled since both the mechanical excitation and the voice coil are connected at the center of the top plate, which is a node of its mode shape.

Secondly, we measured the electrical admittance $Y(\Omega) = \hat{I}(t)/\hat{E}(t)$, as explained in section 4.3, for three values of the negative resistance R_n and without the chopper. We obtained the plots of Fig. 14(b) and estimated the values of the electrical parameters using the model of Eqs. (17), with the mechanical parameters of Tab. 1(b) and $\phi = 2.98$ N/A. We obtained $L = 820$ μH and $C = 3.9$ mF for any values of R_n, giving an electrical natural frequency of $f_e = \omega_e/(2\pi) = 89$ Hz. Then, with $R_n = 0$ (the blue curve of Fig. 14(b)), the total resistance was estimated as $R_L + R_C = 3.16$ Ω. Then, for non zero values of the negative resistance R_n, admittance curves with sharper resonance peaks were obtained. Again, the agreement between theory and experiments is perfect.

5.3. Frequency response with PWM

This section is devoted to the validation of the PWM strategy to artificially change the value of the electrical natural frequency. In the same manner than explained in section 5.2, we measured the electrical admittance $Y(\Omega)$ and the mechanical FRF $H_\gamma(\Omega)$ with the PWM and various values of the duty cycle. Fig. 15 shows the result along with the theoretical response, obtained with the parameter values of estimated in section 5.2 and β_{eff} instead of β (see Eq. (25)). The PWM frequency was set to $f_{\text{PWM}} = 40$ kHz for this experiment, to avoid excessive current ripple in the inductor and the MOSFETs. Again, the agreement between theory and experiments is excellent, by using a slightly lower electrical frequency $f_e = 88.75$ Hz instead of 89 Hz (see the end of section 4.3).

The admittance curves of Fig. 15(a) have been obtained with different negative resistance R_n for each curve, adjusted to obtain almost the same total resistance $R = 1/Y_{\text{max}} \simeq 8$ mΩ, to compensate the change in R due to the PWM, associated to the βR_C term of Eq. (26). The corresponding mechanical FRFs $H_\gamma(\Omega)$ are shown in
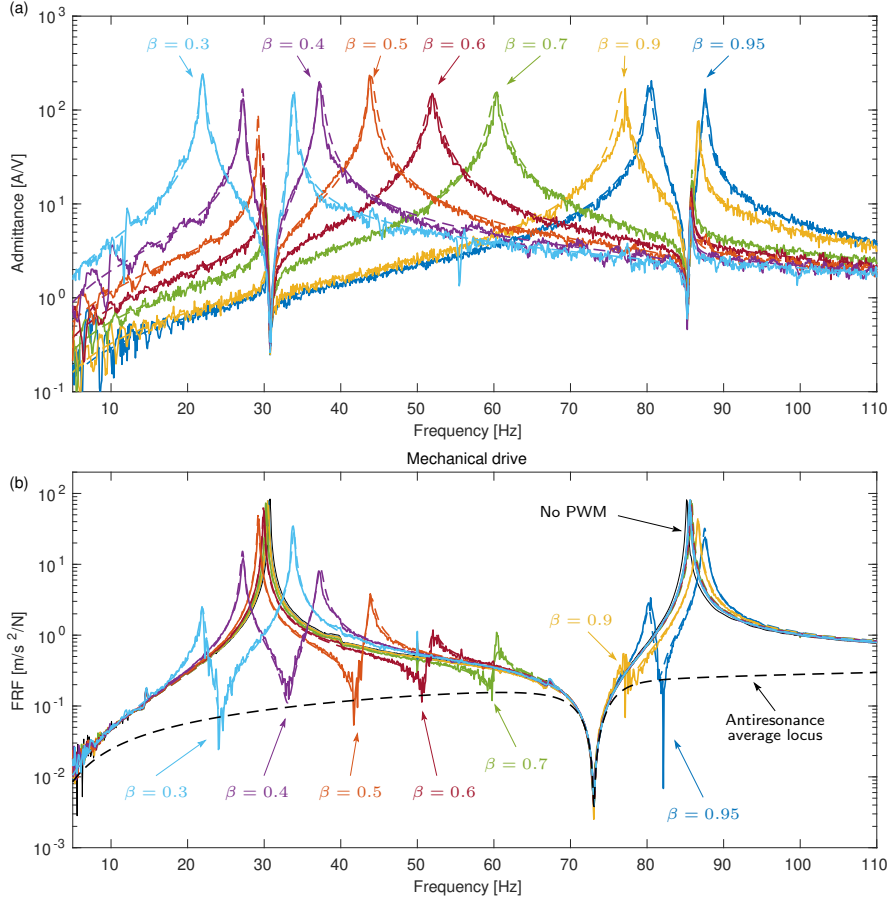
Figure 15. Frequency response as a function of the duty cycle β. (a) Electrical admittance $Y(\Omega)$; (b) Mechanical Frequency Response Function $H_\gamma(\Omega)$; '—': experiments; '--': updated theoretical model.

Fig. 15(b). We can first observe the effect of the two mechanical modes at $f_1 = 30.77$ Hz and $f_2 = 85.35$ Hz, that produce antiresonance in the admittance plots and resonances in the FRF plots. Then, the effect of the duty cycle β changes is clearly visible as it shifts the electrical natural frequency. This latter creates a resonances in the admittance plots and an antiresonance in the FRF plots, that shifts from 24 Hz to 82 Hz as β increases from 0.3 to 0.95. The locus of the antiresonance is also shown with a black dashed line in the FRF plot. It is computed as $H_\gamma(\beta\omega_e)$ for $\beta \in [0,1]$.

The electrical frequency $\bar{\omega}_e$ values have been estimated by picking the frequencies of the antiresonance in Fig. 15(b). They are shown as a function of β in Fig 16. In theory:

$$\bar{\omega}_e = \beta_{\text{eff}}\,\omega_e = (\beta - T_m/T)\omega_e. \tag{28}$$

This theoretical curve, with $T_m/T = 0.025$, is also shown in Fig 16, concluding to a perfect agreement with $f_e = \omega_e/(2\pi) = 88.75$ Hz, the electrical natural frequency already obtained with the fittings of Fig. 15.
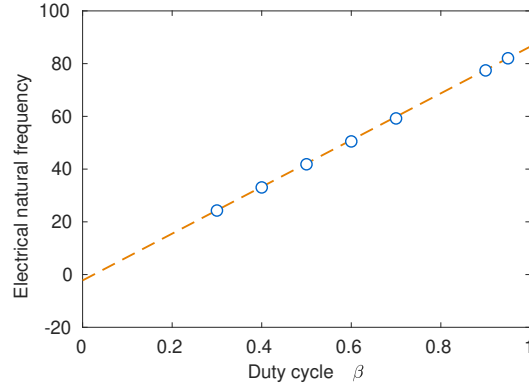
Figure 16. Resonance frequency $\bar{f}_e = \bar{\omega}_e/(2\pi)$ as a function of the effective duty cycle β for the shunted mechanical system with PWM, Fig. 13. 'o': estimation with Fig. 15; '--': theory $\bar{f}_e = f_e(\beta - T_m/T)$.

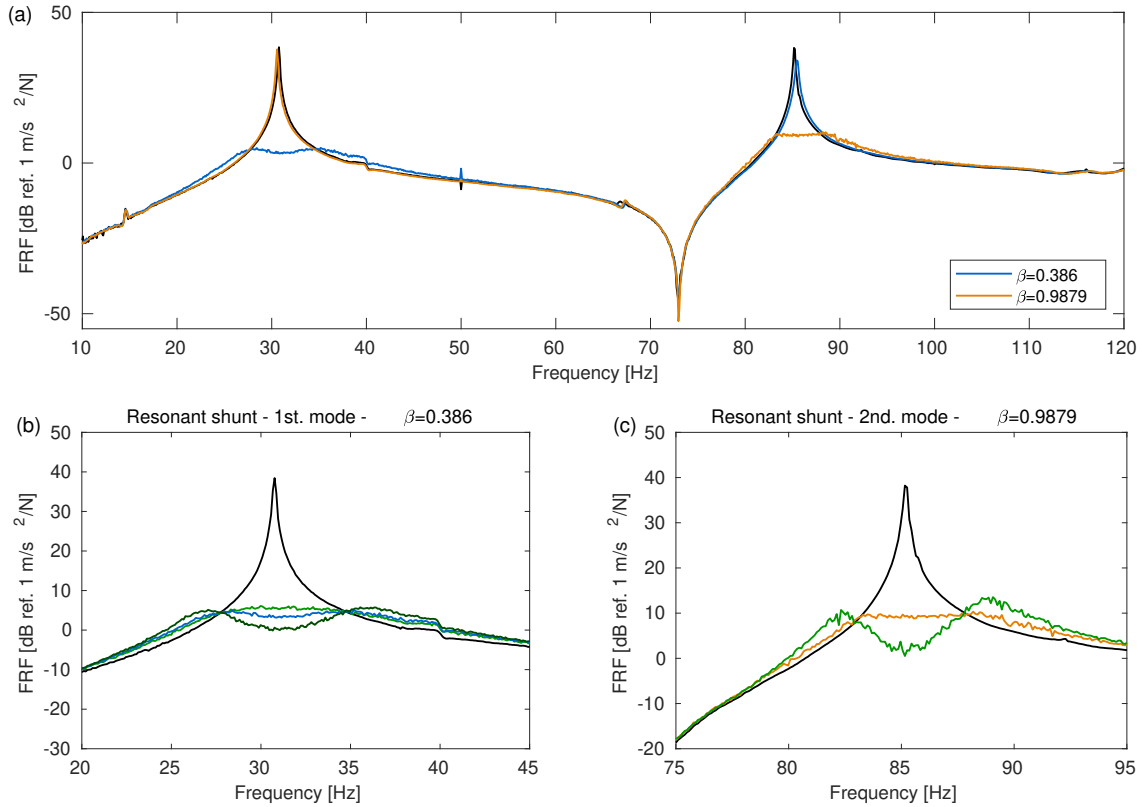## 5.4. Tuned damped resonant shunt with PWM

Figure 17. Damped tuned resonant shunt. Mechanical FRF $H_\gamma(\Omega)$ around the two first resonances of the system with the shunt tuned on the first mode (blue curve) and on the second mode (orange curve). The black curve is associated to the circuit without the chopper. (b), (c): details around the two resonances, with additional curves (green curves) obtained with unoptimal values of the shunt resistance R.

As explained by Eqs. (19) and in various articles (see [9] and reference therein), the two parameters (shunt frequency $\bar{\omega}_e$ and resistance R) of the shunt can be optimally chosen to reduce a given mechanical resonance peak. The experiment was realized and the results are shown on Fig. 17. For the first resonance, this is obtained by first adjusting the electrical frequency through a proper value of the duty cycle ($\beta = \beta_1 = 0.386$), and then by adjusting the negative capacitance R_n to cancel the two side resonances, to obtain a FRF modulus as flat as possible. The same can be obtained for the second resonance, with $\beta = \beta_2 = 0.9879$. This experiment proves the usefulness of the PWM to easily realize a perfectly tuned resonant shunt.

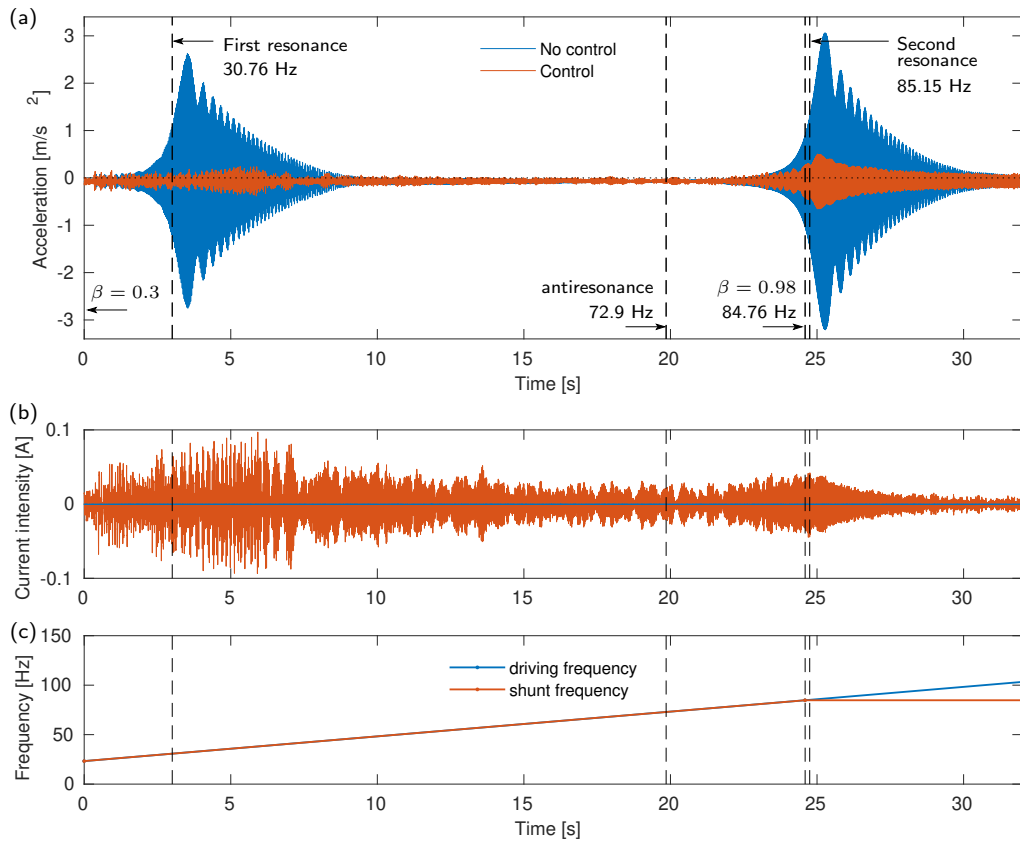## 5.5. Adaptive lightly damped resonant shunt with PWM

Figure 18. Time response of the system without control (with the coil in open circuit, blue curves) and with adaptive resonant shunt control (with synchronized tunable resonant shunt, orange curve), under a sine sweep between. (a) mechanical acceleration response; (b) current intensity in the shunt; (c) evolution of driving frequency and synchronized shunt frequency as a function of time. The times at which the driving frequency reaches the mechanical resonances and the antiresonance of Fig. 14(a) are shown, as well as the time at which the duty factor reaches its maximal value $\beta = 0.98$.

Another use of the tunable resonant shunt can be deduced from Fig. 15. Since the shunt creates an antiresonance at $\Omega = \bar{\omega}_e$ in the mechanical FRF, (see section 3.2 for

the theory), the mechanical response of the structure at this particular frequency is very small. It could be useful in practice if the system is mechanically excited by a harmonic force $F(t) = F_0 \cos \Omega t$. Then, by locking the electrical frequency to Ω with the right value of the duty cycle β (obtained with Eq. (28) inversed), one can think of greatly reduce the mechanical amplitude.

This idea was tested by imposing a slow frequency sweep of the mechanical force and adapting synchronously β with Eq. (28). The chosen sine sweep rate was 2.5 Hz/s, for a sweep duration of 32 s, between 24 Hz and 104 Hz, to sweep a frequency band that include the two first mechanical resonances. For the duty factor law, we chose to not exceed a maximal duty factor of $\beta = 0.98$ (reached at 24.59 s), which, according to Eq. (28), corresponds to an electrical frequency of 84.76 Hz, slightly smaller than the second resonance at 85.15 Hz. After this instant, β was held constant at $\beta = 0.98$ until the end of the sweep. The driving frequency and shunt electrical frequency evolutions are shown in Fig. 18(c).

We recorded the mechanical acceleration $\gamma(t)$ and the current intensity $I(t)$, as shown in Fig. 18(a,b). Without control (*i.e.* with the coil of the EM transducer in open circuit), the blue curve is obtained, showing a large response when the excitation frequency goes trough the two resonances at 30.76 Hz (at 3 s) and 85.15 Hz (at 24.75 s). Those transient responses with beats are typical of a sine sweep going through a sharp resonance. Then, turning the control on (*i.e.* with the tunable resonant shunt connected to the coil), one obtains the orange curve. It is observed that the variations of the envelope of the structural response are greatly reduced: the two resonances are almost canceled, thus reducing the amplitude to an average factor of 40 (equivalent to 32 dB) and validating our control strategy.

One can notice that the second resonance is less attenuated than the first one. This is because of the maximal value of the duty factor $\beta = 0.98$, reached at 24.59 s just before reaching the second resonance, after which the shunt is detuned. One can also notice that a nonzero current intensity $I(t)$ appear when the shunt control is on, since it counteracts the mechanical force applied to the structure. In theory, if the steady state was reached at each instant and the electrical damping was zero, one would have a perfect equality between F and $\phi \dot{Q}$, since $x_i(t)$ would be zero for all i in Eq. (17a), as explained in section 3.2. As a consequence, since the time envelope of the mechanical force is constant, the envelope of $I(t) = \dot{Q}(t)$ would also be constant. In our experiment, Fig. 18(b) shows that this is almost the case, the discrepancy being attributable to the non zero value of the electrical damping and the transient nature of our test.

6. Conclusion

In this article, we presented a novel mean of realizing a tunable electromagnetic shunt absorber using a PWM circuit to continuously change the apparent capacitance – and consequently the electrical frequency – of the shunt. This technique has several advantages. First, it does not changes the intrinsic stability of the resonant shunt: it is

just a mean of changing the apparent value of the shunt capacitance, without injecting external energy into the shunt. It also requires very low additional power, since it is only required to power the switches of the chopper and the controller. Since the DSP used in this article can be realized by a dedicated microcontroller, it is possible to think of a fully passive integrated shunt device that powers its components with harvested energy, as it was proposed earlier for SSD techniques [42].

The main issue of the work proposed here is the residual resistance of the coil of the electromagnetic transducer, which can be large compared to the practical requirements, even for a standard resonant shunt as shown in section 5.4. In this case, a negative resistance has to be added in the circuit. In our study, we used the DSP to synthetize the negative resistance, which can also be realized using analog circuitry with operational amplifiers (see *e.g.* [9]). In this case, the power requirement for the supply of the components is not easy to be estimated and the system could potentially become unstable if the value R_n of the negative resistance is chosen too large, especially in the case of the lightly damped resonant shunt of section 5.5, for which the electrical resistance has to be as small as possible.

7. References

[1] M. D. Rao. Recent applications of viscoelastic dampingfor noise control in automobiles and commercial airplanes. *Journal of Sound and Vibration*, 262:457–74, 2003.

[2] C. Hammami, E. Balmès, and M. Guskov. Numerical design and test on an assembled structure of a bolted joint with viscoelastic damping. *Mechanical Systems and Signal Processing*, 70-71:714–724, 2016.

[3] I. R. Henriques, L. Rouleau, D. A. Castello, L. A. Borges, and J.-F. Deü. Viscoelastic behavior of polymeric foams: Experiments and modeling. *Mechanics of Materials*, 148:103506, 2020.

[4] S. Krenk. Frequency analysis of the tuned mass damper. *Journal of Applied Mechanics*, 72:936–942, 2005.

[5] M. Vakilinejad, A. Grolet, and O. Thomas. A comparison of robustness and performance of linear and nonlinear lanchester dampers. *Nonlinear dynamics*, 100:269–287, 2020.

[6] N. W. Hagood and A. Von Flotow. Damping of structural vibrations with piezoelectric materials and passive electrical networks. *Journal of Sound and Vibration*, 146(2):243–268, 1991.

[7] S. Behrens, A. J. Fleming, and S. O. R. Moheimani. Electromagnetic shunt damping. In *Proceedings of the 2003 IEEE/ASME International Conference on Advanced Intelligent Mechatronics (AIM 2003)*, pages 1145–1150, 2003.

[8] J. A. B. Gripp and D. A. Rade. Vibration and noise control using shunted piezoelectric transducers: A review. *Mechanical Systems and Signal Processing*, 112:259–383, 2018.

[9] M. Auleley, O. Thomas, C. Giraud-Audine, and H. Mahé. Enhancement of a dynamic vibration absorber by means of an electromagnetic shunt. *Journal of Intelligent Materials Systems and Structures*, 2020.

[10] M. Berardengo, S. Manzoni, O. Thomas, and M. Vanali. Piezoelectric resonant shunt enhancement by negative capacitances: Optimisation, performance and resonance cancellation. *Journal of Intelligent Material Systems and Structures*, 29(12):2581–2606, 2019.

[11] O. Thomas, J. Ducarne, and J.-F. Deü. Performance of piezoelectric shunts for vibration reduction. *Smart Materials and Structures*, 21(1):015008, 2012.

[12] R. Darleux, B. Lossouarn, and J.-F. Deü. Broadband vibration damping of nonperiodic plates by

piezoelectric coupling to their electrical analogues. *Smart Materials and Structures*, 29:054001, 2020.

[13] R. D. Middlebrook and S. Cuk. A general unified approach to modelling switching-converter power stages. In *1976 IEEE Power Electronics Specialists Conference*, pages 18–34. IEEE, 1976.

[14] M. H. Rashid. *Power electronics: devices, circuits, and applications*. Pearson, 4th. edition, 2014.

[15] J. J. Hollkamp and T. F. Starchville. A self-tuning piezoelectric vibration absorber. *Journal of Intelligent Materials Systems and Structures*, 5:559–566, 1994.

[16] C. L. Davis and G. A. Lesieutre. An actively tuned solid-state vibration absorber unsing capacitive shunting of piezoelectric stiffness. *Journal of Sound and Vibration*, 232(3):601–617, 2000.

[17] A. J. Fleming and S. O. R. Moheimani. Adaptive piezoelectric shunt damping. *Smart Materials and Structures*, 12:36–48, 2003.

[18] D. Niederberger, M. Morari, and S. J. Pietrzko. Adaptive resonant shunted piezoelectric devices for vibration suppression. In *Smart Structures and Materials 2003: Smart Structures and Integrated Systems*, volume 5056, pages 213 – 224. SPIE, 2003.

[19] D. Niederberger, A. Fleming, S. O. R. Moheimani, and M. Morari. Adaptive multi-mode resonant piezoelectric shunt damping. *Smart Materials and Structures*, 13:1025–1035, 2004.

[20] D. Niederberger, S. Behrens, A. J. Fleming, S. O. R. Moheimani, and M. Morari. Adaptive electromagnetic shunt damping. *IEEE/ASME Transactions on Mechatronics*, 11(1):103–108, 2006.

[21] J. A. B. Gripp, L. C. S. Góes, O. Heuss, and F. Scinocca. An adaptive piezoelectric vibration absorber enhanced by a negative capacitance applied to a shell structure. *Smart Materials and Structures*, 24:125017, 2015.

[22] B. Mokrani, I. Burday, Z. Tian, and A. Preumont. Adaptive inductor for vibration damping in presence of uncertainty. In *Proc. of the 7th ECCOMAS Thematic Conference on Smart Structures and Materials - SMART 2015*, Ponta delgada, Azores, 2015.

[23] T. M. P. Silva, M. A. Clementino, V. C. de Sousa, and C. De Marqui. An experimental study of a piezoelectric metastructure with adaptive resonant shunt circuits. *IEEE/ASME Transactions on Mechatronics*, 25(2):1076–1083, 2020.

[24] L. Dal Bo, P. Gardonio, D. E. Casagrande, and S. Saggini. Smart panel with sweeping and switching piezoelectric patch vibration absorbers: Experimental results. *Mechanical Systems and Signal Processing*, 120:308–325, 2019.

[25] Kaijun Yi, Gaël Matten, Morvan Ouisse, Emeline Sadoulet-Reboul, Manuel Collet, and Gaël Chevallier. Programmable metamaterials with digital synthetic impedance circuits for vibration control. *Smart Materials and Structures*, 29(3):035005, 2020.

[26] Ghislain Raze, Andy Jadoul, Sylvain Guichaux, Valery Broun, and Gaëtan Kerschen. A digital nonlinear piezoelectric tuned vibration absorber. *Smart Materials and Structures*, 29(1):015007, 2019.

[27] T. A. Seer, N. Vahdati, H Karki, and O. Shiryayev. An electromagnetic torsional tuned vibration absorber and its application in rotating equipment. In *Proc. of the ASME 2012 International Mechanical Engineering Congress & Exposition IMECE2012*, Houston, USA, 2012.

[28] S. Miani, M. Zilletti, P. Gardonio, F. Blanchini, and P. Colaneri. Switching and sweeping vibration absorbers: Theory and experimental validation. *Automatica*, 93:290–301, 2018.

[29] C. Richard, D. Guyomar, D. Audigier, and G. Ching. Semi-passive damping using continuous switching of a piezoelectric device. In *Proc. of SPIE Smart Structures and Materials Conference: Passive Damping and Isolation*, volume 3672, pages 104–111, 1999.

[30] W. W. Clark. Vibration control with state-switching piezoelectric material. *Journal of Intelligent Material Systems and Strutures*, 11:263–271, 2000.

[31] P. Shivashankar and S. Gopalakrishnan. Review on the use of piezoelectric materials for active vibration, noise, and flow control. *Smart Materials and Structures*, 29:053001, 2020.

[32] J.-H. Jung, T.-H. Cheng, and I.-K. Oh. Electromagnetic synchronized switch damping for vibration control of flexible beams. *IEEE/ASME Transactions on Mechatronics*, 17(6):1031–1038, 2012.

[33] J. Ducarne, O. Thomas, and J.-F. De. Structural vibration reduction by switch shunting of piezoelectric elements: modelling and optimization. *Journal of Intelligent Materials Systems and Structures*, 21(8):797–816, 2010.

[34] D. Vasic, Y.-P. Liu, and F. Costa. Comparison of piezoelectric structural damping based on velocity controlled switching and pulse width modulation switching circuits. In *proc. of the ASME 2012 International Mechanical Engineering Congress and Exposition - IMECE 2012*, Houston, USA, 2012.

[35] Y.-P. Liu and D. Vasic. Semi-passive piezoelectric structural damping based on a pulse-width modulation switching circuit. *Journal of Mechanical Science and Technology*, 12:3625–3633, 2013.

[36] B. Wang, W. Tang, X. Zheng, Y. Wang, and L. Wang. Adaptive piezoelectric vibration control using pwm based switching power amplifier. In *Proceedings of the 36th Chinese Control Conference*, Dalian, China, 2017.

[37] Q. Mao and S. Huang. Design of tuneable vibration absorber by using inertial actuator with proof-mass acceleration feedback. *International Journal of Structural Stability and Dynamics*, 19(8):1950087, 2019.

[38] C. Giraud-Audine, F. Giraud, M. Amberg, and B. Lemaire-Semail. Generalized modal analysis for closed-loop piezoelectric devices. *Smart Materials and Structures*, 24(8):085028, 2015.

[39] A. Kras and P. Gardonio. Active vibration control unit with a flywheel inertial actuator. *Journal of Sound and Vibration*, 464:114987, 2020.

[40] J. Høgsberg. Consistent frequency-matching calibration procedure for electromechanical shunt absorbers. *Journal of Vibration and Control*, 2020.

[41] O. Thomas, C. Touzé, and A. Chaigne. Asymmetric non-linear forced vibrations of free-edge circular plates, part 2: experiments. *Journal of Sound and Vibration*, 265(5):1075–1101, 2003.

[42] M. Lallart, É. Lefeuvre, C. Richard, and D. Guyomar. Self-powered circuit for broadband, multimodal piezoelectric vibration control. *Sensors and Actuators A*, 143:377–382, 2008.

Appendix A. Derivation of the approximate low frequency dynamics of system with PWM

In this section, we derive the low frequency approximate dynamics of the system of Eqs. (4a,b). Since in those equations $\boldsymbol{x}(t)$ is a continuous time function, one has, at the commutation time $\hat{t}_n$ and t_{n+1} of the PWM, $\forall n \in \mathbb{N}$:

$$
\begin{cases}
\boldsymbol{x}(\hat{t}_n^+) = \boldsymbol{x}(\hat{t}_n^-), & \text{(A.1a)} \\
\boldsymbol{x}(t_{n+1}^+) = \boldsymbol{x}(t_{n+1}^-), & \text{(A.1b)}
\end{cases}
$$

where $\hat{t}_n^-$ and $\hat{t}_n^+$ are instants respectively just before and after switch time $\hat{t}_n$, and the same for t_n^- and t_n^+ with switch time t_n. Formally integrating differential equations (4a,b) leads to:

$$
\begin{cases}
\boldsymbol{x}(t) = \mathrm{e}^{\boldsymbol{A}_1(t-t_n)}\boldsymbol{x}(t_n) + \left(\int_0^{t-t_n} f(\tau)\mathrm{e}^{-\boldsymbol{A}_1\tau}\,\mathrm{d}\tau \right) \boldsymbol{b}_1 & \forall t \in [t_n\ \hat{t}_n], & \text{(A.2a)} \\
\boldsymbol{x}(t) = \mathrm{e}^{\boldsymbol{A}_2(t-\hat{t}_n)}\boldsymbol{x}(\hat{t}_n) + \left(\int_0^{t-\hat{t}_n} f(\tau)\mathrm{e}^{-\boldsymbol{A}_2\tau}\,\mathrm{d}\tau \right) \boldsymbol{b}_2, & \forall t \in [\hat{t}_n\ t_{n+1}], & \text{(A.2b)}
\end{cases}
$$

where we used the variation of constants method to find the particular solution, added to the general solution of the associated homogeneous equation.

We proceed by evaluating the state $\boldsymbol{x}(t_{n+1}^-)$ at the end of the $(n+1)$-th period using Eq. (A.2b), as a function of its value $\boldsymbol{x}(t_n^+)$ at the beginning of the period, by computing $\boldsymbol{x}(\hat{t}_n^+)$ with Eq. (A.2a) just before the switch time, taking into account the continuity condition (A.1a) at the switch time $\hat{t}_n$. One obtains:

$$\boldsymbol{x}(t_{n+1}) = e^{[\beta\boldsymbol{A}_1+(1-\beta)\boldsymbol{A}_2]T}\boldsymbol{x}(t_n)$$

$$+ e^{(1-\beta)T\boldsymbol{A}_2}\left(\int_0^{\beta T} f(\tau)e^{-\boldsymbol{A}_1\tau}\,\mathrm{d}\tau\right)\boldsymbol{b}_1 + \left(\int_0^{(1-\beta)T} f(\tau)e^{-\boldsymbol{A}_2\tau}\,\mathrm{d}\tau\right)\boldsymbol{b}_2. \quad (\text{A.3})$$

We now assume that the PWM frequency $f_{\text{PWM}} = 1/T$ is much larger than the characteristic frequencies of the system, namely the frequencies of the spectrums of $\boldsymbol{A}_1$ and $\boldsymbol{A}_2$. Under this assumption, the following 1st order Taylor expansion is valid:

$$e^{\boldsymbol{A}\tau} = \boldsymbol{I} + \boldsymbol{A}\tau + \boldsymbol{o}(\tau^2). \quad (\text{A.4})$$

Moreover, the frequency content of the forcing function $f(t)$ is also assumed in the low frequency band, $i.e$ much smaller that f_{PWM}, so that one considers $f(t)$ as a constant in a given period T. Then, using Eq. (A.4) in (A.3), taking out $f(t)$ of the integrals and keeping only the linear terms in T, one obtains:

$$\boldsymbol{x}(nT + T) \simeq \left(\boldsymbol{I} + \bar{\boldsymbol{A}}T\right)\boldsymbol{x}(nT) + \bar{\boldsymbol{b}}Tf, \quad (\text{A.5})$$

with

$$\bar{\boldsymbol{A}} = \beta\boldsymbol{A}_1 + (1-\beta)\boldsymbol{A}_2, \quad \bar{\boldsymbol{b}} = \beta\boldsymbol{b}_1 + (1-\beta)\boldsymbol{b}_2. \quad (\text{A.6})$$

Finally, approximating the time derivative of $\boldsymbol{x}(t)$ at time $t \simeq nT$, one has:

$$\dot{\boldsymbol{x}}(t) \simeq \frac{\boldsymbol{x}(t+T) - \boldsymbol{x}(t)}{T} \simeq \bar{\boldsymbol{A}}\boldsymbol{x}(t) + \bar{\boldsymbol{b}}f(t). \quad (\text{A.7})$$

which is Eq. (6).